Chinese Chemical Letters 35 (2024) 109269

Contents lists available at ScienceDirect

Chinese Chemical Letters

journal homepage: www.elsevier.com/locate/cclet

Collaborative integration of Fe-N_x active center into defective sulfur/selenium-doped carbon for efficient oxygen electrocatalysts in liquid and flexible Zn-air batteries

Yufeng Wu, Mingjun Jing*, Juan Li, Wenhui Deng, Mingguang Yi, Zhanpeng Chen, Meixia Yang, Jinyang Wu, Xinkai Xu, Yanson Bai, Xiaoqing Zou, Tianjing Wu*, Xianyou Wang

National Base for International Science & Technology Cooperation, National Local Joint Engineering Laboratory for Key Materials of New Energy Storage Battery, Key Laboratory of Environmentally Friendly Chemistry and Application of Ministry of Education, Xiangtan University, Xiangtan 411105, China

ARTICLE INFO

Article history:
Received 14 August 2023
Revised 3 September 2023
Accepted 31 October 2023
Available online 2 November 2023

Keywords:
Atomic regulation
Chalcogens co-doped
Catalytic performance
Noble metal-free electrocatalyst
Zn-air battery

ABSTRACT

Strategic active site organization is imperative for the advancement of effective and long-lasting catalysts of oxygen reduction reactions. However, the controllable multi-active site design is a highly intricate topic for catalyst synthesis. Employing pre-trapping and post-activation strategy, Fe-N bonding structure and S, Se functionalized heteroatom are integrated into a conductive porous carbon. In this process, the nitrogen-abundant polymer 1,3,5-triformylbenzene-tris(4-aminophenyl)benzene (Tf-TAPA) adsorbs Fe^{3+} under the intrinsically metal anchoring ability of N atoms and simultaneously *in-situ* assembles long-chain thiophene-S. Subsequently, the Fe^{3+} is transformed into Fe-N_x moieties with the conversion of the organic chain to incompletely graphitized carbon. Furthermore, the alteration of the electronic configuration achieved through the introduction of dual-atom S and Se leads to a pronounced enhancement in catalytic efficiency. Benefitting from the Fe-N_x bonding structure, dense structural defects, and conductive carbon networks, the resultant Fe-S,Se/NCNs possesses a positive half-wave potential of 0.86 V and a 90% current retention rate, outstripping the Pt/C benchmark. Moreover, the liquid and flexible ZAB driven by Fe-S,Se/NCNs achieves large power densities of 259.7 and 164.7 mW/cm^2, respectively. This study provides a new comprehension in developing an efficient and stable M-N-C oxygen electrocatalyst.

Efforts to develop efficient energy storage and conversion devices have gained considerable significance in light of the rising energy needs of consumable electronics and electric vehicles [1,2]. Among them, ecological friendliness, safe production, as well as a high theoretical specific capacity (1084 Wh/kg) are satisfactory spotting merits for zinc-air battery (ZAB) [3], thereby being deemed an appropriate candidate in next-generation energy systems. One of the bottlenecks of this apparatus is starved for sluggish reaction kinetics on the air electrode, which terribly weakens the overall electrochemical performance [4–6].

Special transition metals are coordinated with nitrogen moieties to establish a highly proficient catalytic activity through the creation of a robust bonding architecture denoted as M-N-C, where the M encompasses prominent candidates such as Fe, Mn, and Co [7,8]. Especially Fe atoms-nitrogen coordination (Fe-N_x) supported on carbon matrix catalysts is regarded as the most prospective substitute to replace PGM on account of economic affordability, simple fabrication, and attractive catalytic activity. Fe-N_x is generally considered as the real active site for absorbing O_2 and catalyzing the subsequent ORR kinetics [9–11]. A frequently employed technique for the fabrication of Fe-N-C catalysts in conventional systematic synthesis involves the thermal decomposition of carbon, nitrogen, and iron precursors at elevated temperatures. Nevertheless, hybrid thermolysis leads to uncertainties in reference to the amount and location of active sites and a drastic decline in catalytic activity [12]. The use of extra micromolecular nitrogen sources or novel organic nitrogen-containing polymers to trap iron atoms are the universal and valid strategy for high-density active center catalysts. While micromolecular nitrogen sources can cause the collapse or destruction of the microporous structure [13]. The primary limitations of nitrogen-containing polymers also inhabit the deep concealment of a large number of metal centers in a carbon matrix [14,15]. Therefore, it is desired to consider the mor-

---

* Corresponding authors.
E-mail addresses: jingmingjun@xtu.edu.cn (M. Jing), twu@xtu.edu.cn (T. Wu).

https://doi.org/10.1016/j.cclet.2023.109269

phological characteristics of carbon substrate that influence the active site density and accessibility. It should be pointed out that the Fe-N-C catalyst confronts a few deficiencies likewise. There are briefly described below [16–18]: (1) Unitary Fe-N_x sites are limited in efficiency to drive multi-electron and multi-proton transfers. (2) The defect-graphitization tradeoff significantly impacts the catalytic activity and long-term stability of Fe-N_x sites. (3) The excessively strong binding strength between the Fe-N-C active center and the oxygen intermediate will hinder the transfer of protons and electrons. Some attention is paid to adjust the M-N_x local electronic structure by virtue of doping, defect engineering, and ligand modulation, *etc*., which is beneficial to improving their intrinsic ORR catalytic activity [19–22]. When different dopant is introduced into the carbon matrix, the selectable electronic microenvironment is arranged for modular catalyst design. In recent years, *in-situ* modifying the carbon base with sulfur can reduce the d-band center of Fe atoms to lower the adsorption energy [23]. Selenium has similar electronic properties to sulfur, and it can help increase the charge density around Fe-N_x species, thereby enhancing charge transfer and improving conductivity [24]. Apart from implemented modifications affecting the ORR activities, larger size S and Se cause carbon defects and increase surface areas and porosity to make more rapid mass and charge transfer [25]. Moreover, the synergy of multi-heteroatom modification can also enhance oxygen reduction activity to a greater extent [26]. When introducing appropriate heteroatoms into the carbon matrix, it not only triggers a redistribution of the electronic structure but also facilitates the creation of enhanced electrochemically accessible active sites. However, more attempts are needed to regulate Fe-N-C activity by multi-heteroatom modification, and these observations can be further unified for more consistent conceptual guidance.

In this work, we elaborately design uniform F-N_x bonding construction on S, Se co-decorated carbon matrix through pre-trapping and post-activation strategy for efficient ORR. The Fe^{3+} and long-chain thiophene-S species are efficiently fixed onto N-containing polymer 1,3,5-triformylbenzene-tris(4-aminophenyl)benzene (Tf-TAPA) *via* a facile one-pot fabrication. Through subsequent carbonation and selenization processes, a wealth of topological defects are effectively generated, giving rise to the exposure of Fe-N_x species formed *in-situ* within the porous carbon matrix. Taking the advantages of the sulfur-, selenium-functionalized carbon matrix and high activity Fe-N_x moiety, the as-synthesized Fe-S,Se/NCNs achieves excellent ORR catalytic performance.

The synthetic route of Fe-S,Se/NCNs is schematically depicted in Fig. S1 (Supporting information), which involves the polymerization route and two-step annealing step. Control catalysts are prepared using identical methodology, particularly the Se-excluded S-doped nitrogen-carbon matrix (Fe-S/NCNs), and nitrogen-carbon nanospheres (NCNs) obtained by direct thermal decomposition of Tf-TAPA precursor.

The tris(4-aminophenyl)amine and triformaldehyde undergo an *in-situ* Schiff-base reaction to form Tf-TAPA. The prominent stretching vibration at 1625 cm^{-1} confirms the successful formation of C=N groups in Tf-TAPA (Fig. S2 in Supporting information). The polymer Tf-TAPA exhibits a nanosphere morphology with a 200 nm average diameter *via* scanning electron microscopy (SEM) images (Fig. S3 in Supporting information). After carbonization in the Ar atmosphere, the NCNs inherits a spherical morphology (about 150 nm in diameter) and a rough surface in Fig. S4a (Supporting information). As confirmed in Fig. 1a and Fig. S4b (Supporting information), the as-synthesized Fe-S,Se/NCNs and Fe-S/NCNs have distinct 3D cross-linked structures with clear pores and furrows.

The detailed structure is revealed through transmission electron microscopy (TEM). In Fig. 1b, Fe-S,Se/NCNs has loose and rough morphology and no obvious agglomerate iron or nanoparticles, implying the isolation manner metal site. From the high-resolution TEM (HRTEM) image in Fig. 1c, Fe-S,Se/NCNs possesses luxuriant graphene-like wrinkles on the edges, which promotes electrolyte infiltration and supplies a large number of contact points. Furthermore, the observed graphitic carbon layers within the carbonaceous substrate serve as a protective barrier, mitigating the potential corrosion of active species. The elemental mapping exhibits the homogeneous presence of C, N, O, S, Fe, and Se throughout the rough surfaces and wrinkled edges (Fig. S5 in Supporting information).

Through the X-ray diffraction (XRD), a comprehensive investigation into the crystalline structures is conducted (Fig. 1d). The diffraction pattern of Fe-Se,S/NCNs exhibits prominent peaks at 24.3° and 43.6°, originating from the (002) and (100) planes of conventional graphitic carbon, respectively [27]. Similarly, typical reflection planes of carbon material are observed in both Fe-S/NCNs and NCNs. While the carbon characteristic peaks of Fe-S,Se/NCNs have deviated to the left in comparison with NCNs and Fe-S/NCNs. In accordance with the Bragg equation, the displacement is ascribed to a discernible increase in the interlayer spacing among sp^2 carbon layers, achieved through the successful intercalation of Se and S atoms [6,28]. In Fig. 1e, the sp^3 hybridized carbon is denoted by a prominent diffraction peak at around 1347 cm^{-1} (D band), while the sp^2 graphitic carbon is represented by another distinct peak at approximately 1589 cm^{-1} (G band) [29]. Upon multielement modification, the comparatively larger I_D/I_G value (0.93) of Fe-Se,S/NCNs compared to Fe-S/NCNs (0.91) and NCNs (0.88) points to the presence of more topological defects. Additionally, the identification of the 2D band observed in

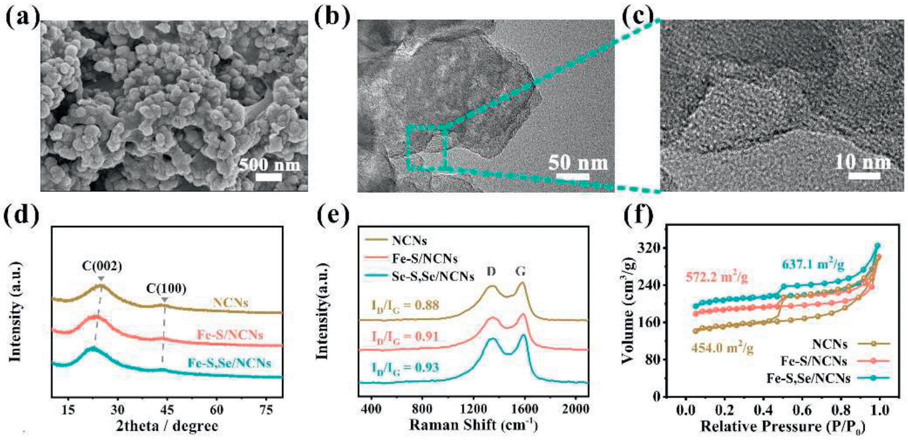

Fig. 1. (a) SEM images, (b) TEM images, (c) HRTEM images of Fe-S,Se/NCNs. (d) XRD patterns. (e) Raman spectrum. (f) N_2 adsorption-desorption isotherms.

Fe-S,Se/NCs indicates the existence of few-layer graphene following the pyrolytic transformation. Consequently, the catalytic performance and durability of Fe-S,Se/NCs are effectively bolstered through the concerted reinforcement of graphitic crystallinity and defect concentration [30–32].

The well-developed porosity and extensive surface area are significant properties for catalytic, and thus, the surface-to-volume ratio and total pore volume of the materials are studied through N_2 adsorption-desorption isotherms. Within the pressure range spanning from low to high (P/P_0), the three samples distinctly exhibit a Type IV isotherm characterized by a well-defined H_4-type hysteresis loop [33], indicating the simultaneous presence of microporous and mesoporous structures (Fig. 1f). The micro-/mesoporosity engenders a robust three-phase interface (gas, liquid, and solid components), augmenting the contact region between the electrode and electrolyte, and facilitating swift mass transfer in the context of the ORR [34]. Concerning BET surface area and total pore volume, the sequence is manifestly ranked as Fe-S,Se/NCNs > Fe-S/NCNs > NCNs (Fig. S6 in Supporting information). With the introduction of S, Se, and Fe, substantial changes in the morphology are able to take place, where the SSA of porous carbon expands from 454.0 m^2/g to 637.1 m^2/g, and the total pore volume increases from 0.184 cm^2/g to 0.271 cm^2/g. Qualitatively, the morphological transformation is confirmed to affect the surface-to-volume ratio. Besides, it can be definitely seen that doping of selenium has the advantage of increasing the micropore surface area.

The structural stability and composition are identified utilizing thermogravimetric analysis (TGA) in the air environment. As shown in Fig. S7 (Supporting information), with the temperature rising, carbon skeleton and iron matter continue to oxidize, and ultimately produce CO_2, H_2O, and other comprehensive products during thermal decomposition, in which the final residue in Fe-S,Se/NCNs is 4.7% Fe_2O_3. Although the TG curve shows a very similar mass loss pathway, the decomposition temperature of Fe-S,Se/NCNs (370.6 °C) is lower than that of NCNs (431.4 °C) and Fe-S/NCNs (376.8 °C). On this subject, more defects and disordered structures in Fe-S,Se/NCNs may have an impact on thermostability [35,36].

The surface element in each of the samples is also exploited by X-ray photoelectron spectroscopy (XPS). In Fig. 2a, the Fe-S,Se/NCNs full survey spectra spots the appearance of C, N, O, S, Se, and Fe signals that match well with the mapping data. The surface elemental composition is summarized in Table S1 (Supporting information). Interestingly, a notable feature is the Fe content increasing from 0.33% in Fe-NSCNs to 0.49% in Fe-S,Se/NCNs. Given the high surface sensitivity of the XPS technique [37–39], the higher surface metal concentration in Fe-S,Se/NCNs corroborates with the increase in microporosities observed in specific surface area, which reflects the key role of Se activators to expose Fe-N_x within the micropores.

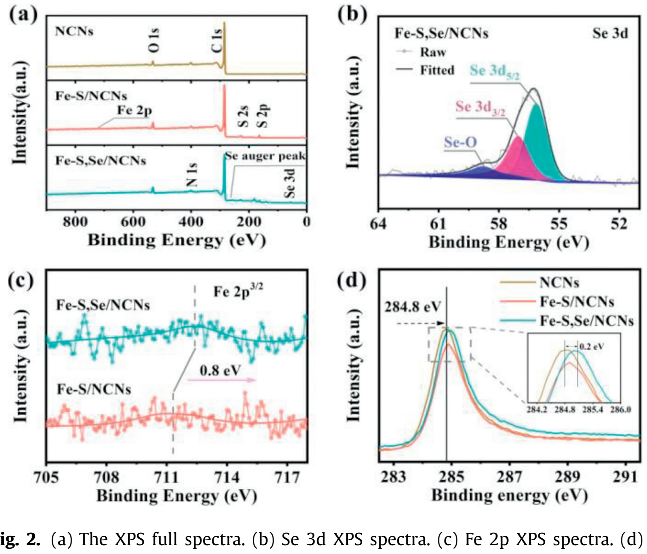

Fig. 2. (a) The XPS full spectra. (b) Se 3d XPS spectra. (c) Fe 2p XPS spectra. (d) C 1s XPS spectra.

High-resolution XPS is provided to present insights into the bonding configurations. In Fig. S8a (Supporting information), the N 1s spectra of NCNs can be divided into four types of contribution belonging to pyridine N, pyrrole N, graphite N, and oxide N, respectively [40,41]. The absolutely high pyridinic/pyrrole sites in NCNs are of significant effects on the coordination operation, and the decrease in pyridinic N and pyrrole N following coordination with Fe species is clearly corroborated in Table S2 (Supporting information). Likewise, a new contribution appeared in both Fe-S/NCNs and Fe-S,Se/NCNs is ascribed to the formation of F-N moieties (Figs. S8b and c in Supporting information). In these circumstances, all the implements adopted forcefully indicate Fe-N configuration instead of agglomerate Fe, the Fe-N_x active sites appear to be rational. In Fig. S9a (Supporting information), the high-resolution S 2p spectrum reveals the signal of thiophene-like C-S-C structure and C-SO_x species presented in Fe-S/NCNs, located at 164.1, 165.2, 167.6, and 168.7 eV, respectively [42]. The previous report highlights thiophene S in governing spin-orbit coupling within the resultant, thereby enhancing the catalytic efficacy of the ORR, while the C-SO_x signal signifies the low activity sulfur oxide [43]. Apart from thiophene structures, the new signal in Fe-S,Se/NCNs is assigned to Se $2p_{3/2}$ and Se $2p_{1/2}$ whose binding energy overlaps with S 2p orbital (Fig. S9b in Supporting information). In Fig. 2b, the high-resolution Se 3d spectrum of Fe-S,Se/NCNs can be resolved well into the predominant C-Se component and weeny Se-O form, corresponding to 56.1, 57.0, and 58.8 eV, respectively [44]. The Fe 2p XPS spectrum in Fig. 2c showcases Fe $2p_{3/2}$ peaks spanning from 705 eV to 718 eV for both Fe-S/NCNs and Fe-S,Se/NCNs, signifying the plausible occurrence of iron in an oxidized state [45]. Worth highlighting is the distinctive phenomenon wherein the band center of Fe-S,Se/NCNs undergoes a discernible redshift of about 0.8 eV relative to that of Fe-S/NCNs. The binding energies characterizing C 1s in the assorted fabricated samples have a discernible shift toward higher binding energies (Fig. 2d). The effects imparted by S and Se dopants are underscored by shifts of 0.2 eV, consecutively manifested in the Fe-S,Se/NCN. This perceptible shift is emblematic of modifications occurring in the vicinity of carbon atoms adjacent to the introduced S and Se dopants. The interplay of S and Se dopants highlights synergistic effects, fostering the promotion of the ORR process [46–50].

According to the prospective properties of the aforesaid introduction, standard three-electrode electrochemical tests are conducted to assess the electrochemical performance. The unmodified counterpart NCNs presents a lower cathode peak at 0.63 V. The Fe-S,Se/NCNs displays a reduction peak at 0.81 V superior to Fe-S/NCNs, and a weeny discrepancy of 0.03 V between Fe-S,Se/NCNs and Pt/C reveals the close ORR catalytic performance (Fig. 3a and Fig. S10 in Supporting information). In Figs. 3b and c, the LSV curve of NCNs has an inferior half-wave potential ($E_{1/2}$) at 0.67 V. Upon Fe and S modification, the $E_{1/2}$ of Fe-S/NCNs significantly increases to 0.72 V. Meanwhile, the Fe-S,Se/NCNs demonstrates a distinct diffusion-limited area and a higher $E_{1/2}$ (0.86 V) than the Pt/C benchmark (0.84 V). Although the limiting current density (J_d) exhibited by the materials remains below the commercial Pt/C, the incorporation of Se emerges as a significant factor contributing to the reinforcement of ORR and electrical conductivity [51,52]. Quantitative evaluations on the Tafel slope are conducted and compared with all materials. In Fig. 3d, the derived Tafel slope of Fe-S,Se/NCNs (55.8 mV/dec) demonstrates the lowest value compared

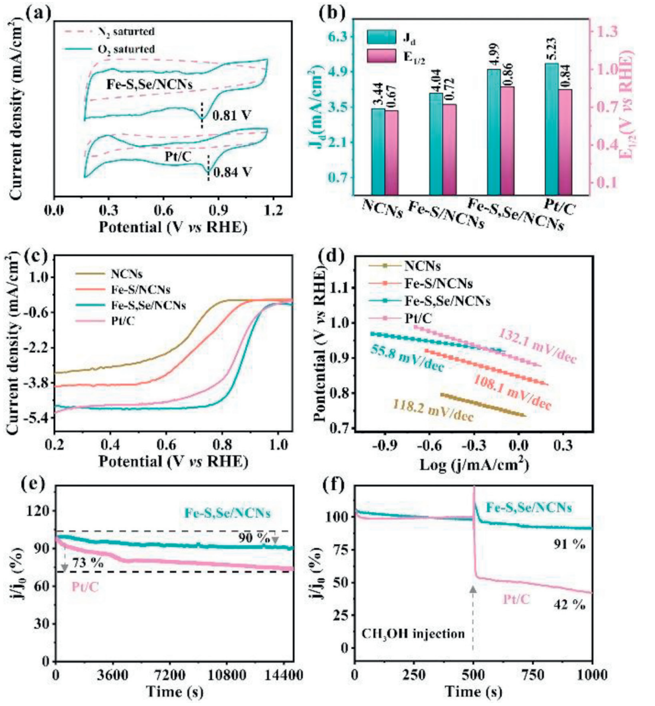

Fig. 3. (a) CV curve. (b) LSV polarization curves. (c) Comparison of $E_{1/2}$ and J_d. (d) Tafel plot. (e) *I-t* curve. (f) The methanol crossover test.

to Fe-S/NCNs (108.1 mV/dec), NCNs (118.2 mV/dec), and the commercially available Pt/C (132.1 mV/dec). The minimum Tafel slope associated with Fe-Se,S/NCNs, relative to alternative catalysts, signifies the presence of more advantageous reaction kinetics during the ORR progression.

The stabilization is represented as another important criterion to weigh the catalytic performance. In Fig. 3e, the current density of Fe-S,Se/NCNs exhibits a 10% reduction in a continuous operation. In contrast, a notable 27% decrease occurs in the Pt/C benchmark after 15000 s, ascribed to the disengagement, inactivation, and migration of Pt nanoparticles from the carbon substrate during operation [53]. In Fig. 3f, the current of Fe-S,Se/NCNs fluctuates marginally upon 3 mol/L methanol addition to 0.1 mol/L KOH, then, rapidly recovers and keeps stable during the 1000 s period. Whereas Pt/C experiences a substantial 48% drop in current retention upon methanol addition. Evidently, the graphitic carbon architecture of the Fe-S,Se/NCNs showcases superior corrosion and oxidation resistance, resulting in pronounced anti-dissolution abilities throughout its operational course. As illustrated in Fig. S11 (Supporting information), the J_d of the Fe-S,Se/NCNs rises with the rotational speed due to the curtate transmission distance and stepped-up mass transfer. According to the Koutecky-Levich (K-L) equation, the corresponding data of Fe-S,Se/NCNs is calculated to obtain an average electron transport number $n \approx 3.9$. Therefore, Fe-S,Se/NCNs possesses high energy conversion efficiency and stability *via* a 4-electron pathway as opposed to a 2-electron pathway [54,55]. The CV curves display a featureless quasi-rectangle in the non-Faraday region, whose area expands with the increasing scanning rate (Fig. S12 in Supporting information). Upon analysis of the C_{dl}, the electrochemical active surface area (ESCA) of Fe-S,Se/NCNs, Fe-NSCNs, and NCNs are calculated to be 12.23, 7.25, and 3.01 mF/cm^2, respectively (Fig. S13 in Supporting information). This observation underscores that the augmentation in the density of adsorption/desorption sites on Fe-S,Se/NCNs can be attributed to the enhancement of surface defects engendered by heteroatom doping.

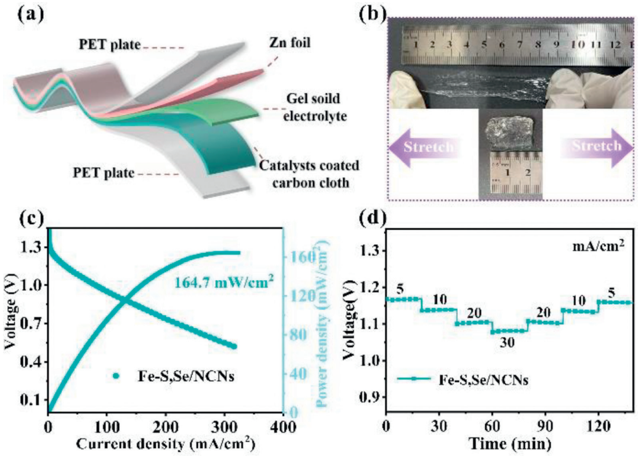

Fig. 4. (a) Schematic illustration of flexible solid ZAB. (b) Photograph of PVA electrolyte. (c) Discharge polarization and power density curves. (d) Rate capability.

However, apart from the impact of S and Se modification on catalytic performance, the catalyst also features the inclusion of metallic Fe-N$_x$ sites. Regarding this aspect, a systematic SCN$^-$ poisoning experiment is carried out to better understand the role of defect structure and Fe-N$_x$ units [4]. In Fig. S14 (Supporting information), the $E_{1/2}$ of NCNs is virtually uninfluential after the SCN$^-$ addition, while the decrease in J_d is ascribed to the positively charged graphite N incorporated with SCN$^-$ through electrostatic attraction. When SCN$^-$ successfully binds the Fe-N$_x$ sites, the $E_{1/2}$ of Fe-S/NCNs and Fe-S,Se/NCNs negatively shift 39 mV and 21 mV, respectively. Furthermore, The sequence of reference catalysts in terms of $E_{1/2}$ and J_d is as follows: Fe-S,Se/NCNs > Fe-S/NCN > NCNs. This finding provides evidence for the considerable defect formation resulting from co-doping with sulfur and selenium, thereby effectively accelerating the catalytic process. Collectively, the superior activity of the Fe-S,Se/NCNs can be related to the following primary features: (1) Appropriate graphitization and defect degree formed in the Fe-S,Se/NCNs improve electronic conductivity and long-term stability; (2) High surface area and porous structure accelerate electrolyte access to active sites; (3) Skillful regulation of atomic Fe doping on the carbon surface ensures the generation of exceptionally valuable and evenly distributed Fe-N$_x$ bonding architectures; (4) Incorporating S and Se atoms into the N-doped carbon framework facilitates the redistribution of carbon charge and spin.

Motivated by urgent requirements for portable equipment of wearable apparatuses, we fabricate flexible ZAB (Fig. 4a). In Fig. 4b, the polyvinyl alcohol (PVA) hydrogel holds a very flexible and bendable nature, and it is stretched to five times as long as the original length without the fracture or breakage, verifying its extraordinary mechanical strength. The flexible solid ZAB powered by Fe-S,Se/NCNs holds a stable OCP of 1.38 V in a 1000 s period (Fig. S15 in Supporting information). As demonstrated in Fig. S16 (Supporting information), the Fe-S,Se/NCNs-base flexible ZAB can maintain an unwavering voltage of 1.38 V when subjected to bending at diverse angles without a significant potential drop. In Fig. 4c, a peak power density of 164.7 mW/cm^2 at 337.4 mA/cm^2 stems from the ZAB driven by Fe-S,Se/NCNs. Fig. 4d shows the Fe-S,Se/NCNs at different discharge current densities from 5 mA/cm^2 to 30 mA/cm^2, respectively. With a gradual increase in current density from 5 mA/cm^2 to 30 mA/cm^2, the battery voltage experiences a slow decline followed by a prompt stabilization. The voltage ultimately reverts to its initial plateau as the current density is gradually reduced. In Fig. S17 (Supporting information), the galvanostatic discharge test at 2.5 mA/cm^2 for 180 min discloses the discharge voltage of Fe-S,Se/NCNs with a small potential change of 0.03 V (from 1.30 V to 1.27 V). These results reveal that Fe-S,Se/NCNs has good catalytic stability and a promising prospect of practical application in wearable ZAB. Moreover, the superiority of this catalyst is confirmed in the context of liquid ZAB, where it exhibits notable discharge stability and a higher peak power density, as indicated in Fig. S18 (Supporting information).

In summary, we successfully prepare multi-component material consisting of Fe-N_x bonding structures and heteroatom (S and Se) functional carbon. Impressively, the Tf-TAPA offers a tough structure and abundant N concentration coordinated with Fe to anchor on a cross-linked structure. The sulfur and selenium access the incompletely graphitized carbon layer to form a number of defect structures and expose the Fe-N_x bonding configuration, which improves the count of active sites. The synergistic effect of dispersed Fe-N_x moieties combined with functionalized S and Se can make more rapid electron transport in the ORR process. Moreover, continuously hierarchical porosity contributes to the enhanced exposure of electrochemistry available sites. Therefore, the as-prepared Fe-S,Se/NCNs has an excellent ORR performance. This work establishes a novel avenue for the design and fabrication of electrocatalysts with efficacy and robustness.

Declaration of competing interests

The authors declare that they have no known competing financial interests or personal relationships that could have appeared to influence the work reported in this paper.

Acknowledgments

This work was supported by Distinguished Young Scholar Fund Project of Hunan Province Natural Science Foundation (No. 2023JJ10041), the Hunan Provincial Education Office Foundation of China (No. 21B0147), the Science and Technology Program of Xiangtan (No. GX-ZD20211004), the Hunan Provincial united foundation (No. 2022JJ50136), the National Natural Science Foundation of China (No. 52003230), the Science and Technology Innovation Program of Hunan Province (No. 2021RC2091).

Supplementary materials

Supplementary material associated with this article can be found, in the online version, at doi:10.1016/j.cclet.2023.109269.

References

[1] D. Zhao, Z. Zhuang, X. Cao, et al., Chem. Soc. Rev. 49 (2020) 2215–2264.
[2] C. Hu, R. Paul, Q. Dai, et al., Chem. Soc. Rev. 50 (2021) 11785–11843.
[3] C.X. Zhao, J.N. Liu, J. Wang, et al., Chem. Soc. Rev. 50 (2021) 7745–7778.
[4] S.K. Singh, K. Takeyasu, J. Nakamura, Adv. Mater. 31 (2019) 1804297.
[5] T. Zhou, H. Shan, H. Yu, et al., Adv. Mater. 32 (2020) 2003251.
[6] K. Wang, Z. Lu, J. Lei, et al., ACS Nano 16 (2022) 11944–11956.
[7] Y. Zhu, K. Yue, C. Xia, et al., Nano-Micro Lett. 13 (2021) 137.
[8] Y. Hong, L. Li, B. Huang, et al., Adv, Energy Mater. 11 (2021) 2100866.
[9] A. Zitolo, V. Goellner, V. Armel, et al., Nat. Mater. 14 (2015) 937–942.
[10] K. Chen, K. Liu, P. An, et al., Nat. Commun. 11 (2020) 4173.
[11] S. Wagner, H. Auerbach, C.E. Tait, et al., Angew. Chem. Int. Ed. 58 (2019) 10486–10492.
[12] F. Lin, Z. Dong, Y. Yao, et al., Adv. Energy Mater. 10 (2020) 2002176.
[13] H. Zhang, H.T. Chung, D.A. Cullen, et al., Energy Environ. Sci. 12 (2019) 2548–2558.
[14] X. Xie, C. He, B. Li, et al., Nat. Catal. 3 (2020) 1044–1054.
[15] J. Tian, A. Morozan, M.T. Sougrati, et al., Angew. Chem. Int. Ed. 52 (2013) 6867–6870.
[16] W. Zhang, Y. Chao, W. Zhang, et al., Adv. Mater. 33 (2021) 2102576.
[17] D. Yu, Y. Ma, F. Hu, et al., Adv. Energy Mater. 11 (2021) 2101242.
[18] Y. Ouyang, L. Shi, X. Bai, et al., Chem. Sci. 11 (2020) 1807–1813.
[19] H. Zhang, H. Guang, R. Li, et al., J. Mater. Chem. A 10 (2022) 21797–21815.
[20] C. Hu, L. Dai, Adv. Mater. 31 (2019) 1804672.
[21] K. Gao, B. Wang, L. Tao, et al., Adv. Mater. 31 (2019) 1805121.
[22] X. Hao, Z. Jiang, B. Zhang, et al., Adv. Sci. 8 (2021) 2004572.
[23] I.-Y. Jeon, S. Zhang, L. Zhang, et al., Adv. Mater. 25 (2013) 6138–6145.
[24] Q. Wu, M. Liu, N. Shang, et al., J. Alloys Compd. 848 (2020) 156367.
[25] Z. Chen, X. Su, J. Ding, et al., Appl. Catal. B 308 (2022) 121206.
[26] T. Oh, M. Kim, D. Park, et al., Appl. Surf. Sci. 440 (2018) 627–636.
[27] D. Menga, J.L. Low, Y.S. Li, et al., J. Am. Chem. Soc. 143 (2021) 18010–18019.
[28] E. Montiel Macias, A.M. Valenzuela-Muñiz, G. Alonso-Núñez, et al., Diam. Relat. Mater. 103 (2020) 107671.
[29] M.A. Ahsan, A.R.P. Santiago, Y. Hong, et al., J. Am. Chem. Soc. 142 (2020) 14688–14701.
[30] Q. Shi, Q. Liu, Y. Ma, et al., Adv. Energy Mater. 10 (2020) 1903854.
[31] B. Wang, Y. Ye, L. Xu, et al., Adv. Funct. Mater. 30 (2020) 2005834.
[32] H. Li, K. Du, C. Xiang, et al., J. Mater. Chem. A 8 (2020) 17136–17149.
[33] Y. Li, T. Jing, G. Xu, et al., Polymer 149 (2018) 13–22.
[34] X. Wan, X. Liu, Y. Li, et al., Nat. Catal. 2 (2019) 259–268.
[35] K. Chen, G. Li, Y. Wang, W. Chen, et al., Green Energy Environ 5 (2020) 50–58.
[36] J. Xu, Y. Lin, J.W. Connell, et al., Small 11 (2015) 6179–6185.
[37] A. Mulyadi, Z. Zhang, M. Dutzer, et al., Nano Energy 32 (2017) 336–346.
[38] M. Mazzucato, G. Daniel, A. Mehmood, et al., Appl. Catal. B. 291 (2021) 120068.
[39] J.J. Wang, X.P. Li, B.F. Cui, et al., Rare Metals 40 (2021) 3019–3037.
[40] Y. Zhou, G. Chen, Q. Wang, et al., Adv. Fun. Mater. 31 (2021) 2102420.
[41] J. Yang, Z. Wang, C.X. Huang, et al., Angew. Chem. Int. Ed. 60 (2021) 22722–22728.
[42] J. Li, S. Chen, W. Li, et al., J. Mater. Chem. A 6 (2018) 15504–15509.
[43] H.W. Liang, X. Zhuang, S. Brüller, et al., Nat. Commun. 5 (2014) 4973.
[44] J. Li, H. Zhang, W. Samarakoon, et al., Angew. Chem. Int. Ed. 58 (2019) 18971–18980.
[45] G. Yasin, S. Ibrahim, S. Ibraheem, et al., J. Mater. Chem. A 9 (2021) 18222–18230.
[46] H.J. Zhang, J. Geng, C. Cai, et al., Chin. Chem. Lett. 32 (2021) 745–749.
[47] X. Zhang, Y. Wang, K. Wang, Chem. Eng. J. 416 (2021) 129096.
[48] H. Hu, J. Wang, B. Cui, et al., Angew. Chem. Int. Ed. 61 (2022) e202114441.
[49] X. Yan, Y. Jia, X. Yao, Chem. Soc. Rev. 47 (2018) 7628–7658.
[50] H. Liu, Q. Liu, Y. Wang, et al., Chin. Chem. Lett. 33 (2022) 683–692.
[51] Y. Jia, X. Xiong, D. Wang, et al., Nano-Micro Lett. 12 (2020) 116.
[52] J.J. Chen, S. Gu, R. Hao, et al., Rare Metals 41 (2022) 2055–2062.
[53] K. Yuan, C. Lu, S. Sfaelou, et al., Nano Energy 59 (2019) 207–215.
[54] X. Wang, Z. Chen, Z. Han, et al., Adv. Funct. Mater. 32 (2022) 2111835.
[55] H. Yang, Y. Liu, X. Liu, et al., eScience 2 (2022) 227–234.